Hydrodynamics and sediment transport in normal weather: examples from a macrotidal tidal flat-channel system, Rudong, Jiangsu

Zhenqiao Liu
East China Normal University
Liming Xue
East China Normal University
Chao Gao
Nanjing University
Benwei Shi
East China Normal University
Ya Ping Wang
East China Normal University
Shu Gao
shugao@nju.edu.cn

Nanjing University

Research Article

Keywords:

Posted Date: July 19th, 2024

DOI: https://doi.org/10.21203/rs.3.rs-4520853/v1

Additional Declarations: No competing interests reported.

Version of Record: A version of this preprint was published at Geo-Marine Letters on December 4th, 2024. See the published version at https://doi.org/10.1007/s00367-024-00787-0.

Hydrodynamics and sediment transport in normal weather: examples from a macrotidal tidal flat-channel system, Rudong, Jiangsu

Zhenqiao Liu [1], Liming Xue [1], Chao Gao [2], Benwei Shi [1], Ya Ping Wang [1,2], Shu Gao [2]

[1]State Key Laboratory of Estuarine and Coastal Research, East China Normal University, Shanghai 200241, China. [2]School of Geographic and Oceanographic Sciences, Nanjing University, Nanjing 210093, China.

Corresponding author: Shu Gao

Abstract

A detailed understanding of the hydrodynamics and sediment transport mechanisms of the intertidal mudflat-channel system can better predict its future survival and development potential. This study selected a typical open-coast macrotidal mudflat, Xiaoyangkou tidal flat in Rudong in the central part of Jiangsu Province, as the studied area, with field observations conducted on the tidal mudflat-channel system during tidal cycles. The study revealed wind waves generated by winds of around 7 m/s within a fetch length of 5 km can cause significant erosion on the mudflats during neap tides. Wind waves cannot cause erosion on the thalweg within the tidal channels and the lower parts of the banks under normal weather conditions. The peak flow velocity in the flood and ebb within the tidal channels occurs below the bankfull depth. Three different types of erosion processes were observed on the channel slopes: (1) Small-scale erosion on slopes of less than 10 cm in width and less than 5 cm in depth, causing widening and deepening of small tidal gullies, leading to vertical erosion of the slopes. (2) Medium-sized tidal creeks with 10-100 cm widths and depths of 5-100 cm experiencing sliding erosion. (3) Large tidal channels with widths greater than 200 cm and depths greater than 100 cm are more likely to toppling collapse. Continuous waves caused by wind oscillations below the bankfull depth at the observed cross-section of the tidal channels may be the main cause of erosion on the channel banks.

Introduction

The intertidal mudflat-channel system is an important component and primary representative in coastal systems (Gao, 2018; Perillo et al., 2024), and it is also a complex coastal geomorphic system. Water, sediments, organic matter, and nutrients exchange and transport within this system (Friedrichs and Perry, 2001; Mann, 2009; Fagherazzi, 2013), with its complex dynamic and biogeomorphic processes forming erosion and accumulation in spatial patterns, profoundly shaping coastal morphologies. Additionally, the coastal wetlands formed by the intertidal mudflat-channel system can exchange and purify water (Spencer and Harvey, 2012; Xin et al., 2022), enhance carbon sequestration (Kelleway et al., 2016), provide habitats for fish and birds (Whitfield, 2017), and reduce wave energy, protecting shorelines (Fagherazzi et al., 2006; Temmerman et al., 2023). However, over the past 40 years, global mudflats have decreased by 16.02% (Murray et al., 2019), a trend that may worsen against the backdrop of rising sea levels and global climate change (Day et al., 2000; Temmerman and Kirwan, 2015). A detailed understanding of the hydrodynamics and sediment transport mechanisms of the intertidal mudflat-channel system can better predict its future survival and development potential.

The sediment transport in intertidal areas is influenced by various dynamic processes, including tidal currents, wave action, wind forces, river inputs, and biological processes (French and Stoddart, 1992; Allen, 2000; Temmerman et al., 2004; Fagherazzi and Wiberg, 2009; Ghinassi et al., 2018). The sediment dynamics in the intertidal zone involve numerous variables, making the process mechanisms highly complex. On unvegetated mudflats in the intertidal zone, the interaction between water flow and the flat surface is more direct due to the absence of vegetation resistance, leading to differences in critical shear stress for erosion and accretion, along with the combined effects of scouring/settling lag influencing sediment processes on tidal flats (Wang, 2012). After tidal channels develop on bare flats, they continuously oscillate and change shape, adjusting their geometric shape and stratigraphy to adapt to local tidal prism changes (Marani et al., 2002; Stefanon et al., 2012; Brivio et al., 2016). The development of meandering can erode and deposit on the channel bank, exacerbating the lateral oscillation of tidal channels (Solari et al., 2002; Finotello et al., 2018). Collapses of the channel bank can also occur on straight tidal channels, reshaping the tidal flat surface (Gong et al., 2018). Subsequently, when the tidal flat reaches a critical elevation,

salt marsh vegetation becomes established, and due to the presence of vegetation, the banks of tidal channels are less susceptible to erosion, stabilizing the tidal channels network (Mudd et al., 2010).

In these intertidal sediment dynamic processes, the role of wind cannot be ignored. Previous studies have conducted a series of research on these processes, with many focusing on the sediment dynamics processes under stormy weather conditions. In high wind conditions, the bottom shear stress generated by waves is the main mechanism causing sediment erosion (Fan et al., 2002; Yang et al., 2003; Zhu et al., 2016; Xie et al., 2017). Some scholars have also conducted research on the evolution of intertidal landforms under normal weather conditions (Shi et al., 2017; Colosimo et al., 2020). However, research on the complete system of intertidal flats and tidal channels under normal weather conditions is relatively limited at present. It is still unclear how wind affects the geomorphological evolution of the intertidal flat-channel system under normal weather conditions. Therefore, studying the intertidal flat-channel system can provide a more intuitive observation of the impact of wind on the geomorphological evolution processes and mechanisms of the system, which is helpful for understanding the developmental evolution of tidal channel systems in the early to middle stages.

On the central coast of Jiangsu, there are extensive intertidal mudflats (Wang, 1983; Chen et al., 2016). The tidal range along these mudflats is often greater than 4m, with the width of the shore perpendicular to the coast ranging from several kilometers to over a dozen kilometers (Zhang et al., 1992). The mudflats are covered with fine-grained sediment and have relatively gentle slopes (Gao and Zhu, 1988). A large number of tidal channels have developed on the tidal flats in central Jiangsu, with these channels exhibiting rapid oscillation rates (Zhao et al., 2022). The rapid geomorphological changes provide support and convenience for our observational activities.

In this study, we conducted tidal-scale field observations of the mudflat-channel system in Rudong, Jiangsu, using hydrodynamic instruments and a 3D laser scanner. The aim of this research was to investigate the sediment dynamics of a muddy macrotidal mudflat-channel system under the influence of wind during normal weather conditions. The specific research objectives were twofold: (i) to determine the impact of wind on the evolution of intertidal flat landforms, (ii) to reveal the evolution process of the intertidal flat-channel system under normal weather conditions

Material and Methods

Study Area

The field observation site of this study is located at Xiaoyangkou intertidal flat in Rudong, Jiangsu. Rudong is located on the southern part of the radial sand ridge off the Jiangsu coast, where silt-sand tidal flats have developed (Fig. 1.a). The tidal flat consists of three zones from land to sea: salt marsh-Spartina alterniflora flat, mud-sand mixed flat, and sandy flat (Zhu and Xu, 1982). The sediment is mainly composed of sandy silt and silty sand, with an average grain size of 3.0 Φ - 5.8 Φ.

The annual average temperature in Rudong is 16.1°C, with an annual average precipitation of 1045 mm. Northerly winds dominate in winter and southeasterly winds prevail in summer. The annual average wind speed is 6.8 m/s, and the annual average relative humidity is 75.8% (Zhang et al., 2022). The dominant wave direction in the Rudong sea area is N (NNE) with a frequency of 27.5%, and the NE direction is the strong wave direction, with a measured significant wave height of up to 4.20 m and a maximum wave height of 6.9 m.

The Rudong sea area experiences regular semidiurnal tides with large tidal ranges, averaging 4.61 m and reaching over 8 m in maximum tidal range. The tidal currents are mainly bidirectional, with the mainstream direction ranging from 240° to 300° during flood tide and from 70° to 100° during ebb tide (Zhao and Gao, 2015). The flood and ebb tidal currents are nearly symmetrical in speed and duration. The average duration of flood tide in the study area is approximately 5 hours and 55 minutes, while ebb tide lasts around 6 hours and 28 minutes. The flood tide current speed ranges from 0.85 to 1.06 m/s, and the ebb tide current speed ranges from 0.69 to 1.14 m/s, with a maximum difference in flood and ebb tide current speeds exceeding 0.5 m/s (Cao and Yang, 2006).

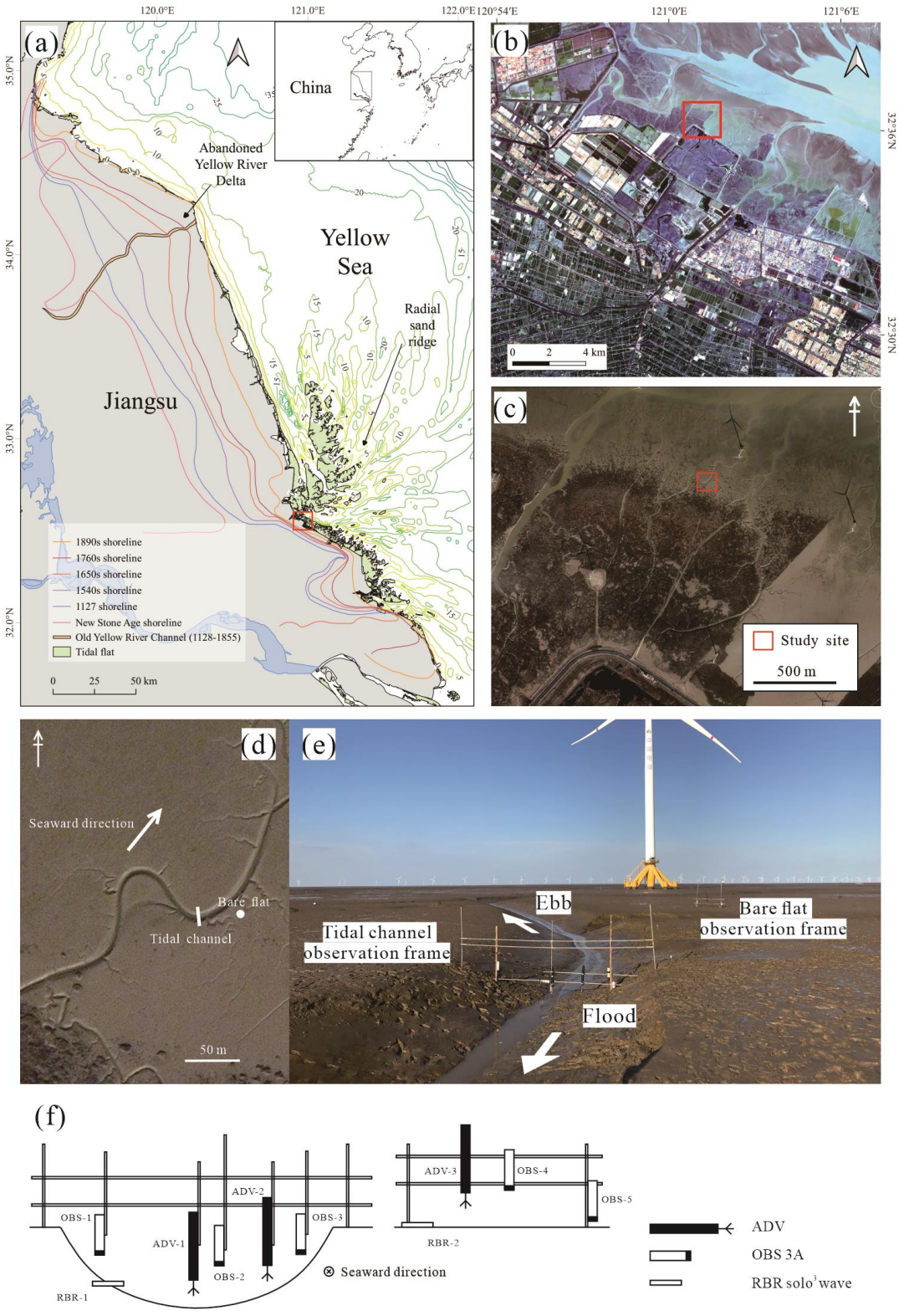

Fig. 1 Study area. (a) The Jiangsu coast faces the Yellow Sea and features a large-scale developed radial sand ridge. Rudong is located on the southern of the radial sand ridge. (b) The XiaoYangkou tidal flat, Rudong County, Jiangsu Province, China (satellite image: PSB, SD, 13 March 2024). (c) The study site is located on the mudflat at the front edge of the salt marsh at Xiaoyangkou, where

the vegetation in the salt marsh is dominated by *Spartina alterniflora Loisel* (map data: Google, TerraMetrics, 14 December 2021). (d) Specific locations of the observation stations at tidal channel and bare flat. (e) Picture of the observation site. (f) Instruments deployment

Field Measurements and data collection

This study was conducted from October 12 to 22, 2020 at a monitoring site located outside the reclaimed dike of Xiaoyangkou, Rudong, Jiangsu Province, China (Fig. 1b). The site is situated in an open tidal salt marsh - mudflat transitional zone (Fig. 1(c,d)). Waves, tidal currents, suspended sediment concentrations (SSCs) and intratidal bed-level changes were observed using acoustic Doppler velocimeter (ADV, Nortek, Norway), wave gauge (RBR solo^3 wave, Ruskin, Canda), and optical Backscattering Sensor (OBS-3A; Washington, USA) (Fig.1f). The observation instruments were mounted on a custom-made gate-type observation frame, with two stations set up for synchronous observation, located at the tidal channel and mudflat (Fig.1e). Two ADVs were installed respectively at the thalweg and bank above the tidal channel, while another ADV was set up above the mudflat. Detail parameter descriptions and sampling settings can be found in Table 1. ADV utilizes the principle of acoustic Doppler to measure high-frequency three-dimensional point velocity data at a certain distance in front of the probe. Besides, ADV can also measure intratidal bed-level changes (Salehi and Storm, 2012; Shi et al., 2015; Zhu et al., 2016). RBR wave employs a piezoresistive pressure sensor to measure water depth and wave information. OBS-3A uses an optical probe to infer water turbidity, which can be converted into suspended sediment concentration data through subsequent indoor calibration. OBS-1, OBS-2 and OBS-3 are at the same elevation. During the filed observations, weather data were obtained from Rudong Meteorological Station.

Table 1 Summary of instrumentation and deployment information

Instruments	Distance of the probe from the bed/cm	Parameters		
		Frequency /Hz	Cycle/min	Samples
ADV-1/ADV-2/ADV-3	20	16	5	4096
OBS-1/OBS-2/OBS-3	30	1	2.5	30
OBS-4	70	1	2.5	30
OBS-5	5	1	2.5	30
RBR-1/RBR-2	20	4	5	1024

A three-dimensional Terrestrial Laser Scanner (TLS, Riegl VZ4000, RIEGL, Austria) was used to conduct terrain scanning at the observation site during the study (Fig. 2a). The Riegl VZ4000 scanner has an effective scanning distance of approximately 2300 m, an accuracy of 15 mm, a resolution of 10 mm, a near-infrared laser wavelength, a laser beam divergence of 0.15 mrad, and scanning angles ranging from ±30° in the vertical direction and 0°-360° in the horizontal direction. The angular resolution is 0.002°-0.280° in the vertical direction and 0.002º-3º in the horizontal direction (Riegl, 2015).

A three-dimensional laser scanner was mounted at a height for observation (Fig. 2b), and retroreflective control point targets were arranged at the observation site. The positions of the laser scanner and the center point of the retroreflective control point targets were measured using RTK-GPS to unify the point cloud data into the coordinate system of the control network for coordinate correction, achieving absolute coordinate acquisition of the point cloud data.

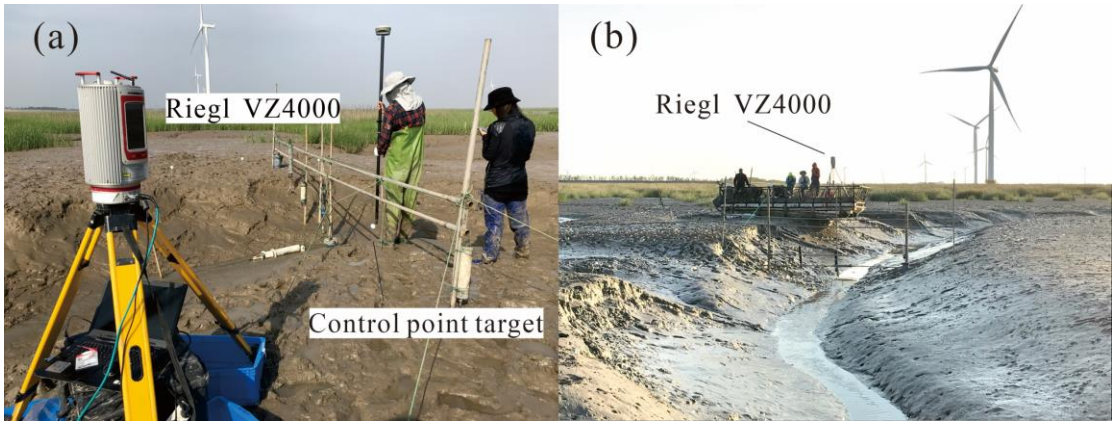

Fig. 2 TLS and control point target(a). Picture of scanning positions(b)

Data Post-Processing

Bed shear stress due to waves

The bottom shear stress τ_w (N/m^2) induced by waves is primarily determined by the wave orbital velocity U_δ (m/s) of water particles and the friction coefficient f_w. The calculation formula is as follows (Soulsby, 1995):

$$\tau_w = \frac{1}{2}\rho_w f_w U_\delta{}^2 \tag{1}$$

Where ρ_w is the density of seawater (kg/m^3), the peak orbital velocity of wave water particles (U_δ) and the peak orbital excursion (A_δ) can be expressed as:

$$U_\delta = \omega A_\delta = \frac{\pi H}{T\sinh(kh)} \tag{2}$$

$$A_\delta = \frac{H}{2\sinh(kh)} \tag{3}$$

Where H is the wave height (m), $k = (2\pi/L)$ is the wave number (m^{-1}), L is the wavelength, T is the wave period (s), g is the acceleration due to gravity (m/s^2), and $\omega = (2\pi/T)$ is the angular velocity (s^{-1}). The calculation formula for the friction factor in equation (1) is as follows (De Swart and Zimmerman, 2008):

$$f_w = \min\{\exp[-6 + 5.2(\frac{A_\delta}{2.5d_{50}})^{-0.19}], 0.3\} \tag{4}$$

Where d_{50} (μm) is the median grain size of sediment on the bed surface, taken as the observed value of 50 μm in this case.

Current-induced bed shear stress

The current-induced bed shear stress is calculated using the second momentum vertical turbulent kinetic energy method (TKEw) (Kularatne and Pattiaratchi, 2008; Shi et al., 2015). Energy spectrum analysis (ESA) (Soulsby and Humphery, 1990) was used to decompose the wave velocities from the turbulent velocities. The high-frequency three-dimensional point current velocity U obtained from ADV observations in the field can be decomposed into three orthogonal instantaneous flow velocities. The water flow on tidal flats is influenced by bottom friction, forming a near-bed turbulent boundary layer. In the boundary layer, the current velocity can be decomposed into mean

current velocity ($*^{-}$) and fluctuating current velocity ($*^{'}$), with the fluctuating current velocity ($*^{'}$) further decomposed into wave orbital motion component ($*_w$) and turbulent component ($*_t$): $u = \bar{u} + u_w + u_t$, $v = \bar{v} + v_w + v_t$, $w = \bar{w} + w_w + w_t$; u, v, w are the magnitudes of the instantaneous flow velocities in the three orthogonal directions of U.

Turbulent kinetic energy (TKE) can be expressed as:

$$TKE = \frac{1}{2}\rho_w(\overline{u_t^2} + \overline{v_t^2} + \overline{w_t^2}) \tag{5}$$

The TKEw vertical turbulent kinetic energy method calculates the bed shear stress $\tau_{c,TKEw}$ (N/m^2) generated by the current as:

$$\tau_{c,TKEw} = C_2\rho_w\overline{w_t^2} \tag{6}$$

Where: C_2 is a constant, taken as 0.9 (Kim et al., 2000), ρ_w is the density of seawater.

Combined wave and current shear stress

The current direction φ_c is calculated through the mean current velocity horizontal component $\bar{u}$ and $\bar{v}$, and the wave direction φ_w is determined by calculating the wave trajectory current velocity u_w and v_w . The direction with the highest frequency in a single instrument pulse is defined as the wave direction φ_w .

The combined wave-current shear stress on the bed τ_{cw} (N/m^2) is calculated using the Soulsby and Clarke (2005) model:

$$\tau_{cw} = \sqrt{\left(\tau_m + \tau_w\left|\cos\varphi_{cw}\right|\right)^2 + \left(\tau_w\left|\sin\varphi_{cw}\right|\right)^2} \tag{7}$$

where φ_{cw} is the angle between the current direction φ_c and wave direction φ_w , and τ_m is the average bed shear stress.

$$\tau_m = \tau_c[1 + 1.2(\frac{\tau_w}{\tau_w + \tau_c})^{3.2}] \tag{8}$$

Results

Wind, tides, currents and waves

The meteorological conditions during the observation period are shown in Fig. 3a Throughout the observation period, the predominant wind direction was onshore, with the overall wind direction ranging between NNE and NE, and an average wind speed of 3.46 m/s. The maximum wind speed occurred at 10:00 on October 14, with a speed of 7.32 m/s, while the minimum wind speed was recorded at 1:00 on October 21, with a speed of 0.10 m/s.

The highest significant wave heights observed on the bare flat and in the tidal channel both occurred at the T4 tidal period (Fig. 3.c), with a maximum significant wave height of 0.37 m on the bare flat and 0.26 m in the tidal channel. The maximum wave energy on the bare flat was 100.93 J/m^2, while in the tidal channel it was 48.63 J/m^2 (Fig. 3d).

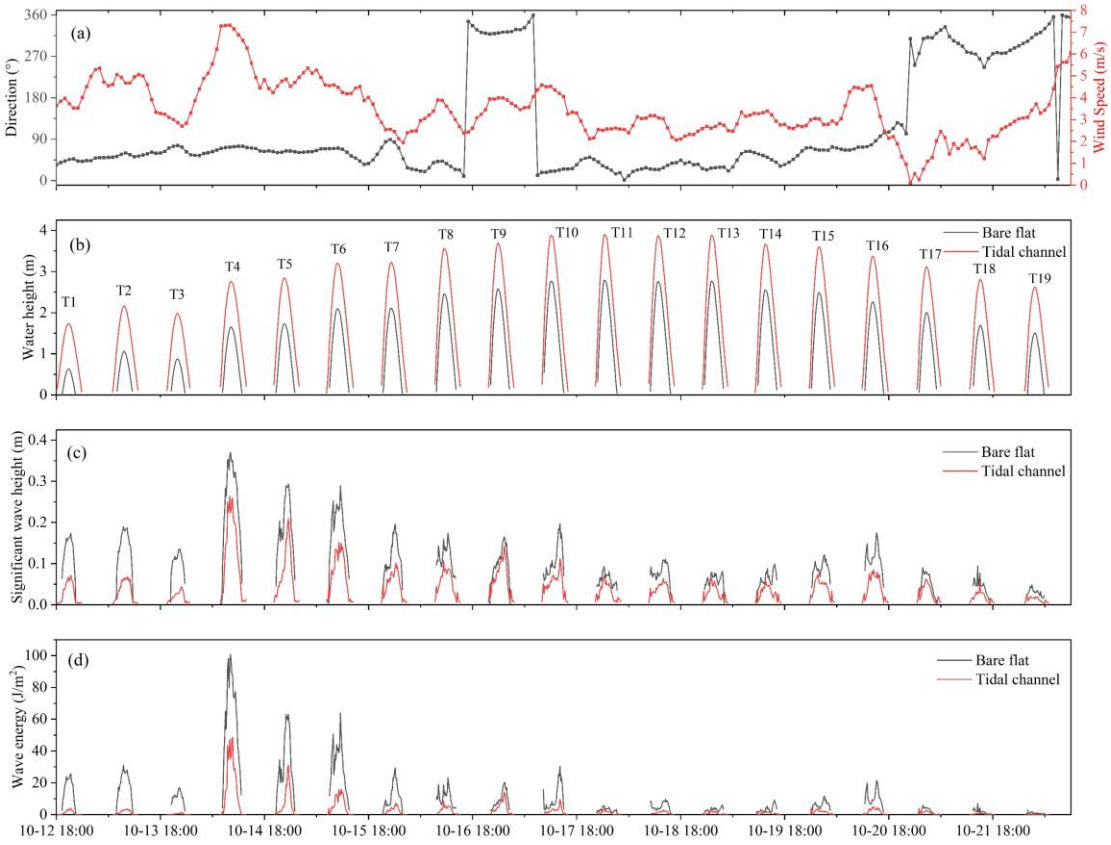

Fig. 3 (a) Hourly wind speed. (b) and (c) water height and significant wave height during the study period (12 October–22 October 2020). (d) Wave energy during the study period. Wind data were obtained every hour from Rudong Meteorological Station. The annotations T1–T19 in Fig. 5b indicate the tides during field measurements.

Current velocity, water height, shear stress and SSCs over the entire observation period are presented in Fig. 4. Valid data from the ADV located above the cut bank at the bottom of the tidal channel was only recorded during the T1-T4 and T12 tidal cycles due to instrument malfunction.

The tidal cycle alternated between neap and spring tides. The highest water depth during the spring tide was 3.90 meters at the channel thalweg and 2.79 meters at the bank, recorded at 00:30 on October 18th during the T11 cycle. The neap tide's maximum depth was 1.74 meters at the thalweg and 0.64 meters at the bank, noted at 20:50 on October 12th in the T1 cycle. The channel's average submergence time was 319.5 minutes, ranging from 350 to 370 minutes, while the bare flat averaged 249.5 minutes, with a range of 190 to 280 minutes (Fig. 4a).

Peak current velocities in the tidal channel showed the maximum flood tide velocity at 1.06 m/s during T15 and the minimum at 0.43 m/s during T1. The highest ebb tide velocity peaked at 0.83 m/s during T5 and dipped to 0.49 m/s during T2. On the intertidal flat, flood tide velocities peaked at 0.45 m/s during T4 and dropped to 0.15 m/s during T2, while ebb tide velocities reached a high of 0.42 m/s during T11 and a low of 0.19 m/s during T19 (Fig. 4d).

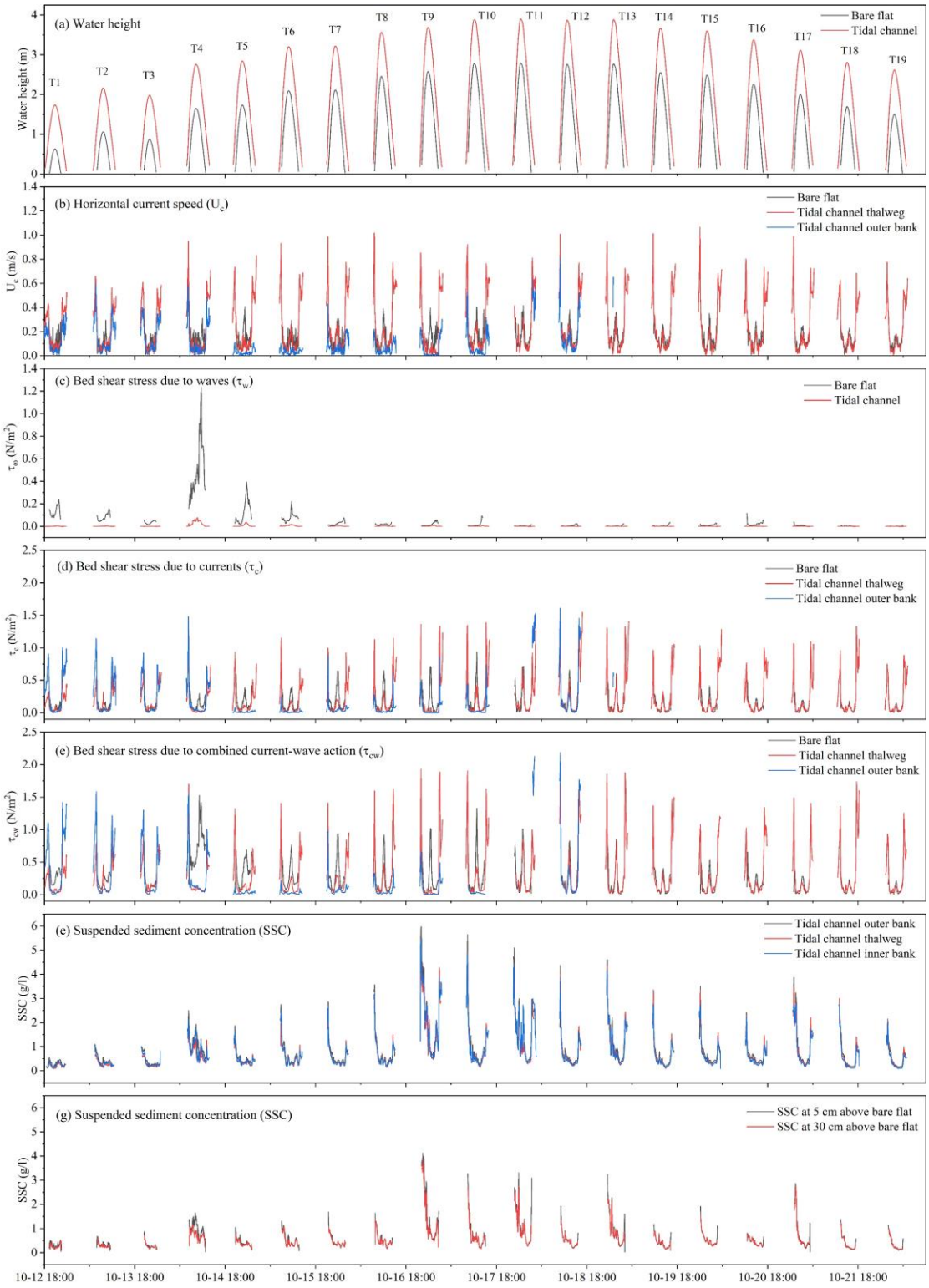

Fig. 4 Time series at mudflat and tidal channel: (a) water height; (b) mean horizontal current velocity 5 cm above the bed; (c) bed shear stress due to waves (τ_w); (d) bed shear stress due to currents (τ_c); (e) bed shear stress due to combined current-wave action (τ_{cw}); (f) and (g) SSC in the tidal channel and on the mudflat.

Fig. 5a and 5b illustrate substantial variations in water levels and current velocities between tidal channels and intertidal flats. In intertidal flats, water levels and current velocities demonstrate consistent relationships across tidal cycles. During neap tides, current velocities for both flood and ebb tides remain stable despite water level fluctuations. Conversely, during spring tides, flood tide velocities are typically lower than ebb tide velocities around the flood peak.

At tidal channel sites, peak current velocities for both flood and ebb tides are observed below bankfull depth, with flood tide velocities exceeding those of the ebb tide. When water levels rise above bankfull during flood tides, current velocities in tidal channels decrease sharply, aligning with velocities observed at comparable water levels during ebb tide. After the flood peak, as water levels recede to bankfull, ebb tide velocities in the tidal channel become lower than those on intertidal flats but increase markedly as the water level continues to drop.

Fig. 5c and 5d depict the dynamics of water level change rates at both sites. At tidal channels, the greatest water level change rates occur around the bankfull depth, with higher rates during flood tides compared to ebb tides. The maximum rate of water level change during ebb tides coincides with the return to bankfull depth. Contrarily, at intertidal flats, the maximum water level change rates during flood tides happen at higher water depths compared to ebb tides, with flood tide rates surpassing those of ebb tides.

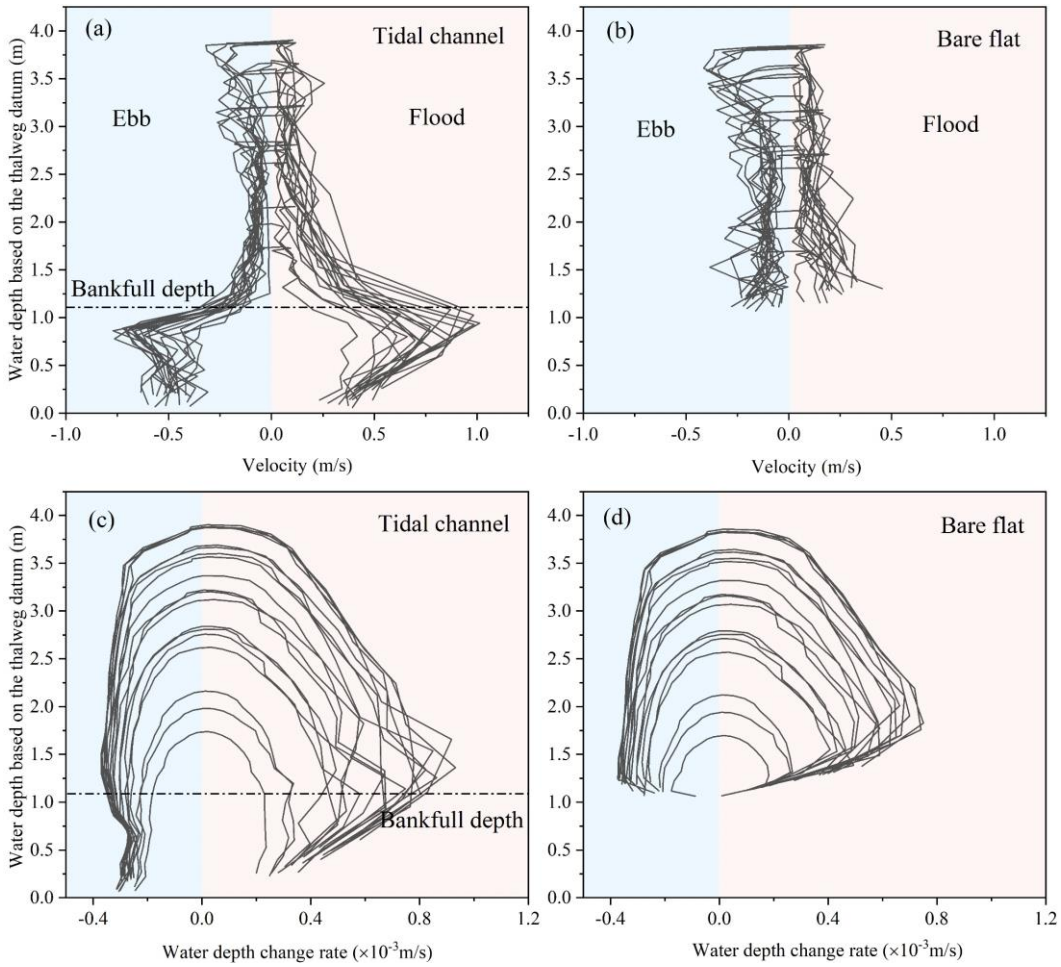

Fig. 5 Relationships between velocity, water depth, and water-depth change rate on the tidal flat station and in the tidal channel station. Red and blue quadrants represent data obtained during the flood and the ebb phase, respectively. For the purpose of comparison, the water depth on the tidal flat is determined based on the observed positions of the tidal channel thalweg. (a) and (b) Plot of current velocity versus water depth for the period of observation. (c) and (d) Plots of water depth and water-depth change rate over the period of observation.

In the tidal channel, consistent current velocities and directions are observed, as illustrated in Fig. 6 comparative analysis of the horizontal composite current velocities and directions at heights above 20 cm on the thalweg and above the channel bank was conducted for neap tide T1, spring tide T12, and medium tide T4. Results indicate that within these cycles, current velocities at the thalweg consistently surpass those at the bank, with both flood and ebb tide velocities exceeding those during slack tide.

During identical meteorological conditions, maximum velocities for both flood and ebb tides

during the spring tide T12 were notably higher than those recorded during the neap tide T1. Slack tide velocities within the channel remained relatively uniform across the T12 and T1 cycles, ranging from 0 to 0.2 m/s. For the medium tide T4, the maximum velocities recorded on the channel slope were 0.59 m/s for the flood tide and 0.50 m/s for the ebb tide, which are higher than those during the neap tide (0.28 m/s and 0.36 m/s) and comparable to the spring tide T12 (0.81 m/s and 0.52 m/s). Notably, during T4, the maximum flood tide velocity in the thalweg was 0.36 m/s greater than at the bank, a difference that exceeded the 0.2 m/s difference observed during T12.

Regarding current directions, significant reciprocating flow characteristics were noted during both the T1 and T12 cycles, predominantly aligning at 90° during flood tide and 270° during ebb tide, which corroborates the directional descriptions in Fig. 2. However, the T4 cycle exhibited notable directional fluctuations within the channel, spanning from 90° to 270°, stabilizing to initial orientations only at the onset of the flood tide and the cessation of the ebb tide.

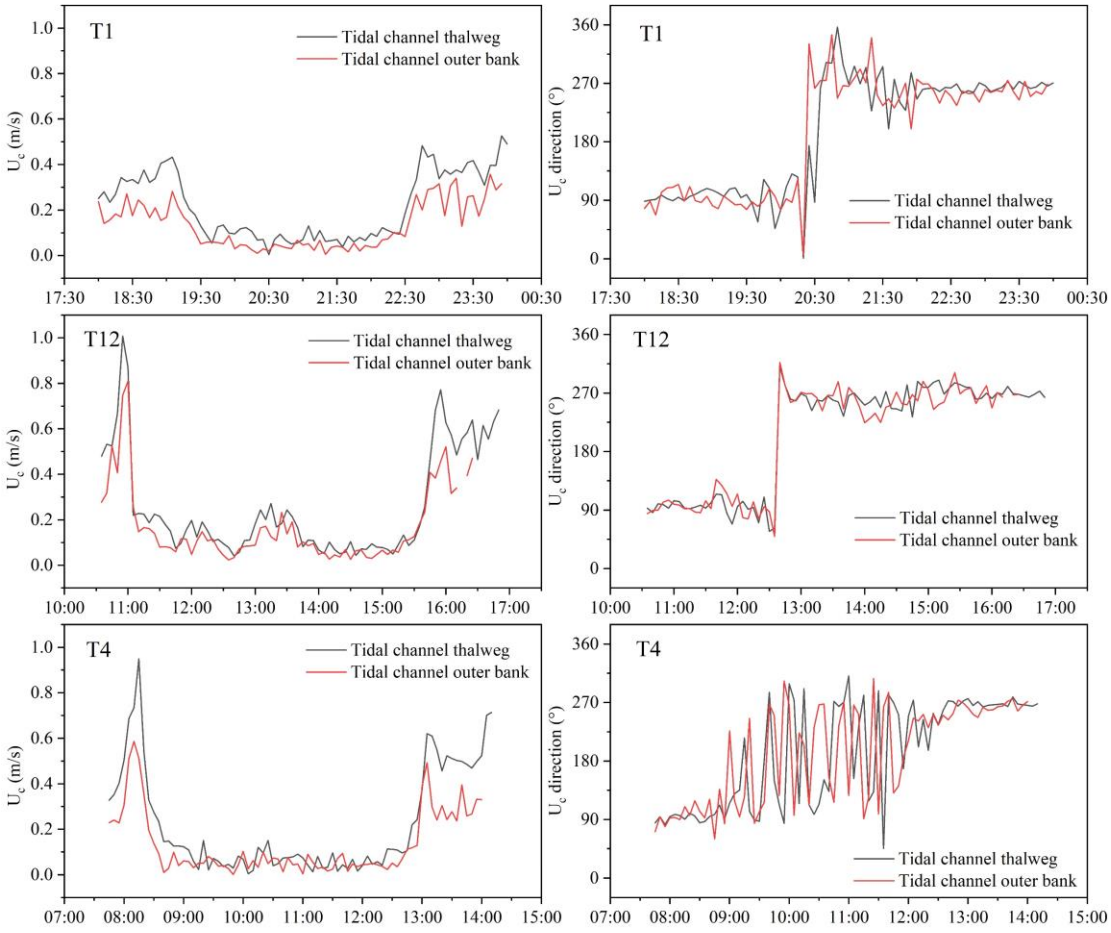

Fig. 6 Internal flow velocities and current directions in tidal channels during different tide cycles

Bed shear stress

During T1 to T19 tidal cycles, maximum bed shear stress due to waves τ_w peaked during T4, closely linked with wind speed variations. Within a single cycle, both flood and ebb phases saw the highest stresses, with the intertidal flat exhibiting greater stresses than the tidal channel, ranging from 0.01 to 1.23 N/m² and 0.001 to 0.08 N/m², respectively. The maximum τ_w during the T4 ebb phase at the intertidal flats was 1.23 N/m², significantly higher than the 0.08 N/m² at the tidal channels.

For current-induced bed shear stress τ_{c-TKEw}, the maximum τ_{c-TKEw} during T4 at the intertidal flat was 0.47 N/m² at rising tide and 0.28 N/m² at falling tide. In contrast, the tidal channel's thalweg saw 1.17 N/m² τ_{c-TKEw} at rising and 0.74 N/m² τ_{c-TKEw} at falling tide, while the bank experienced 1.48 N/m² τ_{c-TKEw} at rising and 0.71 N/m² τ_{c-TKEw} at falling tide.

The combined stress from waves and currents τ_{cw} reached its peak during T4 at the tidal flat, recording a maximum of 1.53 N/m². This stress trend at the tidal channel thalweg mirrored water level changes, peaking at 1.99 N/m² during spring tides, with a notable 1.70 N/m² during T4. The highest bank stress occurred during T12 at 2.19 N/m², exceeding the thalweg's during neap tides.

Analyzing single tidal cycle shear stresses (Fig. 7), T1 (neap tide) showed maximum τ_{cw} of 1.11 N/m² and 1.40 N/m² at the bank during flood and ebb stages, respectively, with lower stresses at the thalweg (0.40 N/m² and 0.61 N/m²) and even lower on the intertidal flat during slack tide (0.14 to 0.42 N/m²). T4 (mid-tide) presented a τ_{cw} range of 1.55 N/m² at the bank to 1.70 N/m² at the thalweg during flood, and 1.01 N/m² at the bank to 0.76 N/m² at the thalweg during ebb, with intertidal flat stresses peaking at 1.53 N/m² during ebb. T12 (spring tide) had the highest τ_{cw}, with the channel bank and thalweg reaching 2.19 N/m² and 1.99 N/m² during flood, and 1.77 N/m² and 1.67 N/m² during ebb, showing an increased τ_{cw} trend during slack tide across locations.

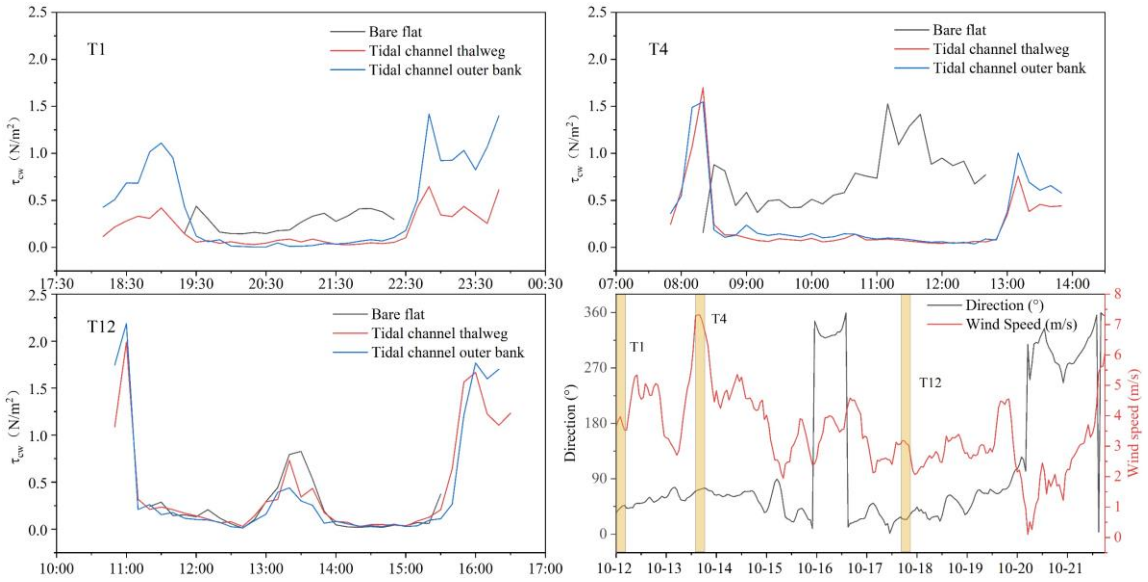

Fig. 7 Combined wave and current shear stresses and wind conditions at stations during different tidal cycles

Suspended sediment concentrations and sediment transport

SSC (Suspended Sediment Concentration) variations at intertidal flat and tidal channel sites correlate with water level changes across semidiurnal and fortnightly tidal cycles, as depicted in Fig. 4g and f Observations during the T4 and T17 cycles show small fluctuations, with higher SSCs generally at the tidal channel than the intertidal flat. SSC profiles typically exhibit a "U" shaped curve within tidal cycles, peaking during flood and ebb tides compared to lower slack tide values. The flood tide SSCs are usually higher, with notable exceptions during T4.

Regarding spatial distribution, SSCs were analyzed at different stations within the tidal channel and intertidal flat across T1, T4, and T12 cycles (Fig. 8). The tidal channel consistently recorded higher SSCs at the outer bank compared to the thalweg and inner bank, except during ebb stages. The highest SSCs at intertidal flats occurred during flood and ebb tides of T1 and T12, with reductions during slack tide.

Comparative data reveal maximum SSC discrepancies between the outer and inner banks during flood stages of 0.19 g/l for T1, 0.6 g/l for T4, and 0.35 g/l for T12. During ebb stages, differences were 0.01 g/l for T1, 0.59 g/l for T4, and 0.11 g/l for T12. Notably, T4's slack tide phase showed significant SSC increases, with differences of 0.23 g/l for T1, 0.63 g/l for T4, and 0.22 g/l for T12 (Table 2). This trend was similarly noted during T1, as shown in Fig. 8, though variations in vertical SSC scales affect direct comparability of magnitude.

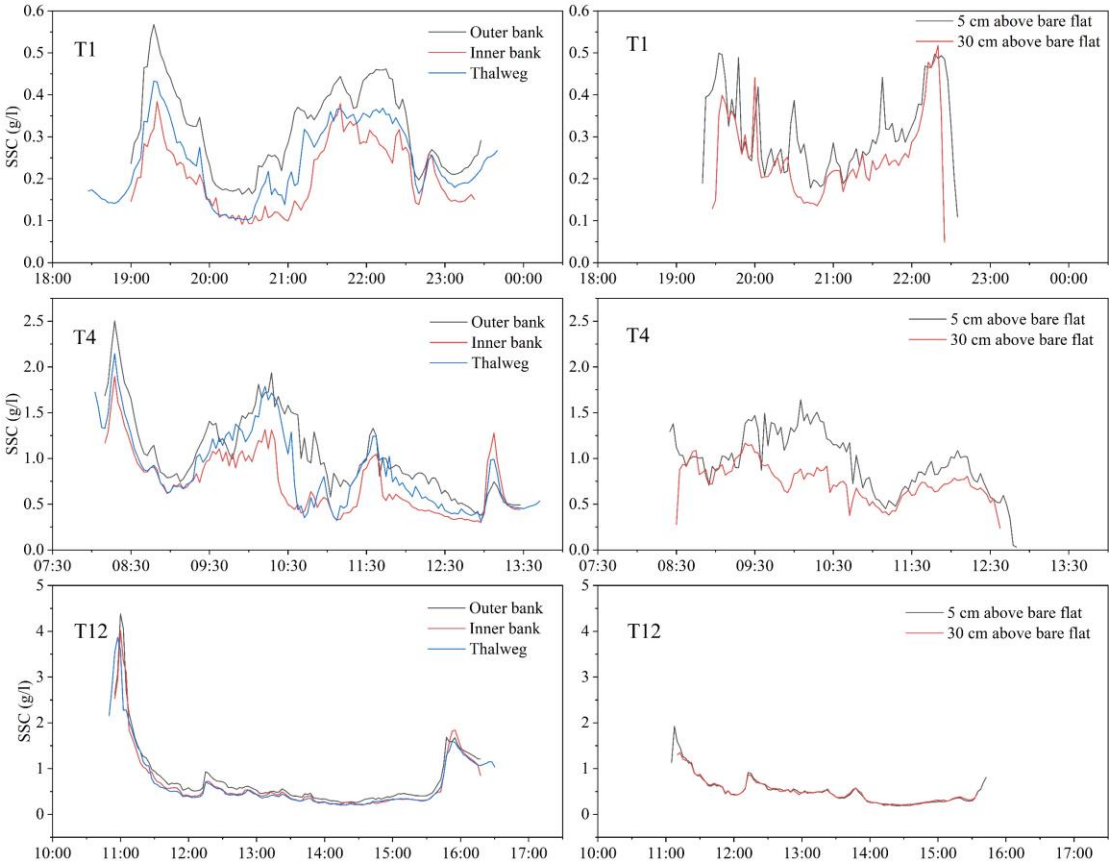

Fig. 8 Time series of SSC for different tidal cycles

Table 2 Maximum SSC at different tide cycles for both flood and ebb stages

Tide cycle	T1		T4		T12	
Maximin SSC（g/l）	Flood	Ebb	Flood	Ebb	Flood	Ebb
Inner bank	0.57	0.27	2.50	0.69	4.37	1.69
Thalweg	0.43	0.26	2.15	0.98	3.87	1.59
Outer bank	0.38	0.26	1.90	1.28	4.02	1.58
5 cm above bare flat	0.50	0.49	1.29	1.01	1.93	0.70
10 cm above bare flat	0.38	0.52	1.09	0.77	1.35	0.47

Bed level change

The ADV's bottom acoustic sensors effectively measured the relative distance from the bottom (Fig. 9), maintaining a consistent elevation of 20 cm throughout the observation period, aligning with measurement requirements. During the study, data indicated that the ADV probe over the tidal

channel thalweg experienced a general erosion trend, with the transducer distance increasing from 220 mm to 280 mm. This trend was punctuated by notable changes during sneap tides (erosion) and spring tides (accretion), particularly during the T4 and T16 tidal cycles. The T4 cycle likely involved cyclic sediment deposition and removal, while T16 changes may have resulted from sediment block movements at the channel bottom.

At the outer bank, data from the T1 to T4 cycles were reliable, but subsequent readings were compromised due to instrument malfunctions, showing no significant erosional or accretional changes during these cycles. At the intertidal flat, erosion was observed during the T4 cycle, followed by notable sedimentation in later cycles, accumulating approximately 25 mm of sediment.

Overall, the measured changes in transducer distance over time depict a dynamic intertidal flat-channel system characterized by phases of erosion, rapid sediment recovery, and accretion, accompanied by a general deepening of the channel bottom.

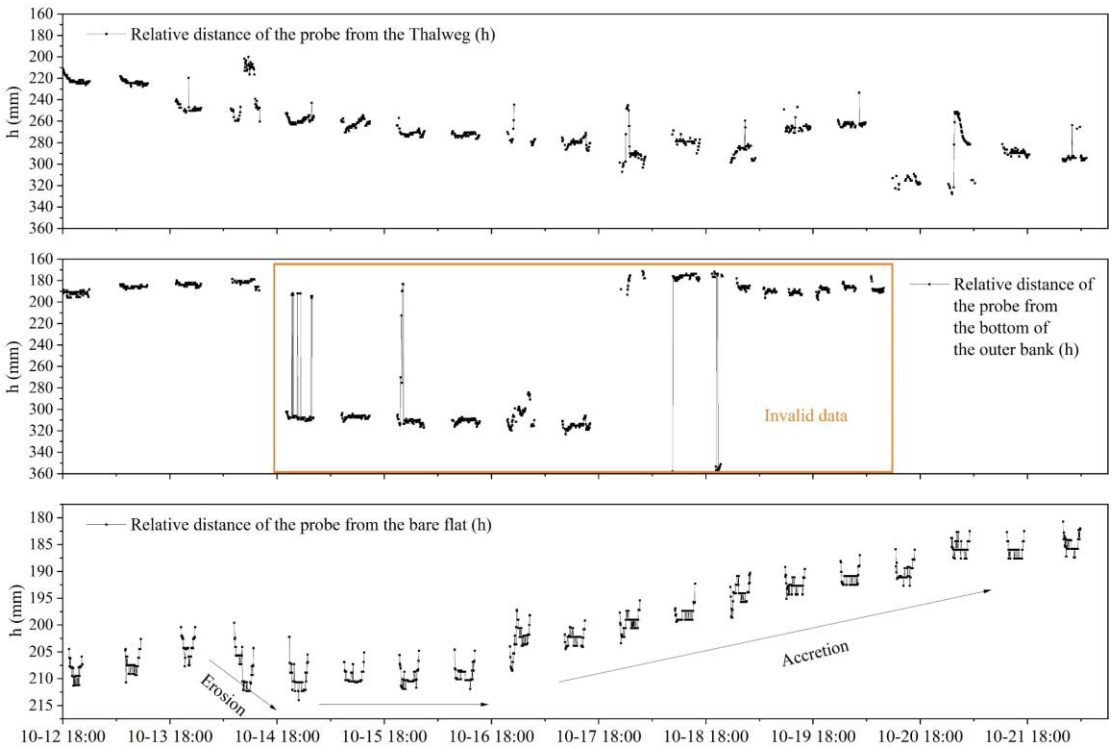

Fig. 9 Bed relative elevation change in the tidal channel and on the bare flat

Lateral tidal channel bank dynamics from TLS

The effective scanning distance of Riegl VZ4000 is approximately 2300 m, with an accuracy of 15 mm and a resolution of 10 mm. Due to the normal weather conditions throughout the entire

observation period, the on-site observation results show no significant sedimentation changes. However, after the scanning data undergo point cloud thinning, interpolation, and DEM generation, a significant decrease in resolution is observed when comparing sedimentation changes. Simply using the interpolated raster for elevation change calculations cannot objectively reflect sedimentation changes (Fig. 10).

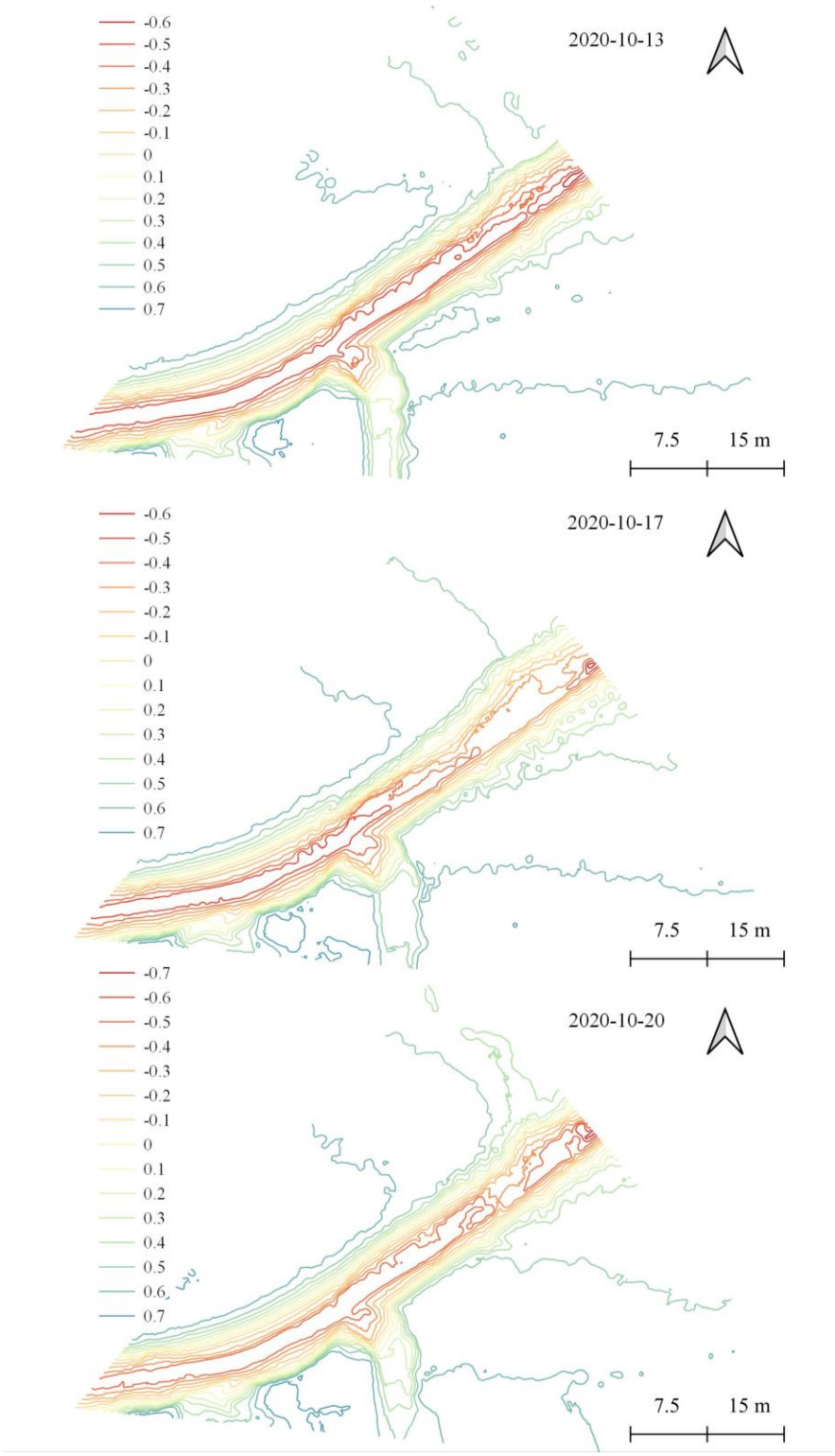

Fig. 10 Topographic elevation of the observation area

Fig. 10 reveals that most areas of the tidal channel exhibit parallel contour lines at various elevations, suggesting a consistent slope from the channel bottom to the intertidal flat. However, fan-shaped areas with noticeable slope variations are evident, particularly in regions captured in

field photographs. For detailed analysis, three representative cross-sections (A, B, C) from the meandering sections were selected (Fig. 11a), each marked on DEMs and actual photographs (Fig. 11b).

Cross-section A features a collapsed bank on the outer side and a smoother transition on the inner bank. Cross-section B shows gentle slopes on both banks, with a notably smaller slope above the outer bank. Cross-section C displays fan-shaped collapses similar to section A's outer bank on both its banks, though the outer bank has a larger collapse area.

Over an 8-day period, overall terrain changes in the tidal channel were minimal, with consistent elevations across the tidal flats on both sides. Specific observations include:

Cross-section A: Notable retreat and accumulation were observed on the outer bank from October 13 to 20, 2020. The retreat measured 16 cm with sediment blocks collapsing top-down, and maximum accumulation in the middle reaching 6-7 cm. The inner bank saw slight erosion at its lower part, about 3 cm deep (Fig. 11c).

Cross-section B: The outer bank experienced varied acceleration, with the upper part, having a smaller slope, showing greater acceleration (5 cm) compared to the lower part (3 cm). The inner bank exhibited no significant erosion or acceleration (Fig. 11d).

Cross-section C: Both banks showed significant fan-shaped collapse, with the outer bank retreating up to 32 cm and the inner bank up to 23 cm, indicating a larger collapse on the outer bank (Fig. 11e).

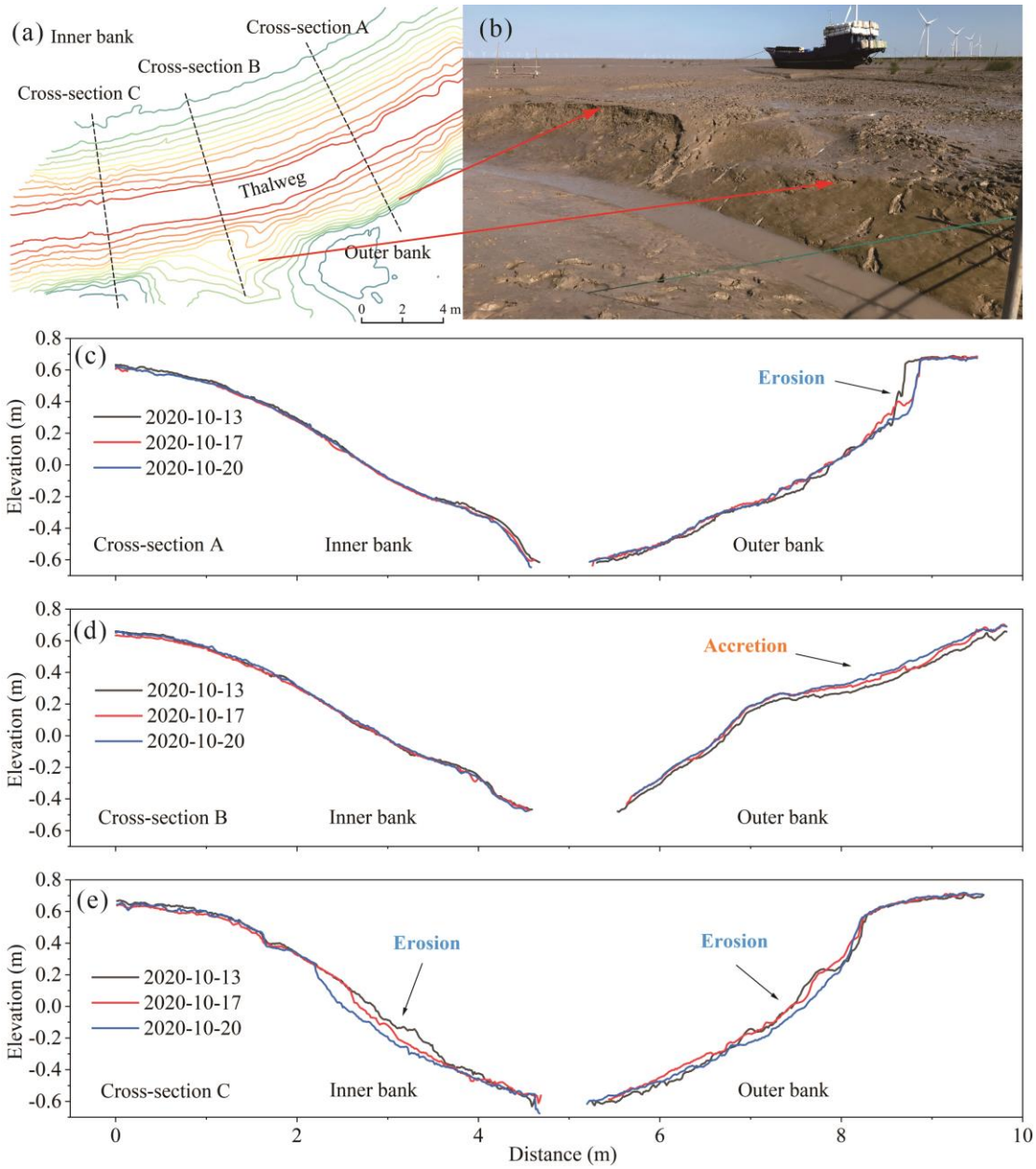

Fig. 11. Elevation changes of tide channel cross section

Discussion

Effects of changing wind conditions on sedimentary dynamical processes on tidal flats and tidal channels during normal weather conditions

In studies of tidal flat sedimentary dynamics, many scholars have observed the impact of changes in wind conditions on tidal flat topography. The action of wind can affect the timing of tides, control resuspension processes, increase wave turbulence energy, and more (Christiansen et al., 2006; Talke and Stacey, 2008; Green, 2011; Colosimo et al., 2020; Shen et al., 2023). In extreme

events such as typhoons or storm surges, this situation can worsen, as the intensification of winds and waves may increase wave trajectory speeds, consequently increasing the bed shear stress caused by waves. Additionally, higher wind speeds can increase the current velocity of the tide, leading to greater bed shear stress from the flow. When the shear stress exceeds the critical shear stress of the bed, erosion of the bed occurs (Yang et al., 2003). In such cases, significant erosion and sedimentation changes can occur in tidal flat topography, and some small-scale tidal channels may experience avulsion (Xie et al., 2017). After the event, the tidal flat can gradually recover.

The magnitude of wind conditions has different impacts on the sedimentary dynamic processes of tidal flat landforms. Under normal weather conditions, changes in wind conditions mainly affect waves. According to linear wave theory, the orbital velocity of waves is influenced by factors such as tidal range, wave period, and water depth (Dean and Dalrymple, 1991).

In this study, the maximum bed shear stress due to waves observed during the T4 tidal cycle on the intertidal flat was 1.53 N/m^2. Although high background suspended sediment concentrations near the bed were observed during the T4 tidal cycle, as shown in Fig. 4, it can be seen that the wave-current shear stress during the slack tide period did not decrease. Instead, there was a sustained higher-than-usual shear stress during the ebb tide period, exceeding any other tidal cycle within the observation period, indicating that the hydrodynamic conditions during this period did not weaken. Combining the observations of maximum SSCs at heights of 5 cm and 30 cm during the T4 tidal cycle, which did not exceed 2 g/l, and maximum wind speeds of only 7.33 m/s, it can be concluded that the observed phenomena were not indicative of the occurrence of a flocculent layer typical in open-coast strong tidal environments (Dyer et al., 2004).

Considering the sustained high SSCs and bed elevation changes recorded by the ADV during the T4 tidal cycle, it can be inferred that erosion occurred on the intertidal flat. Erosion persisted throughout the entire T4 tidal cycle, and in subsequent tidal cycles, the intertidal flat re-aggraded to its pre-erosion elevation.

For the inner part of tidal channels, both the position of the thalweg and the outer bank position observed significantly higher wave-induced shear stresses during the T4 tidal cycle. However, in comparison to the T12 tidal cycle during spring tides, there was no significant increase in the maximum shear stress within the tidal channel during the T4 tidal cycle. Elevated SSCs were observed during the T4 tidal cycle, but there was no observed increase in the bedform migration

distance recorded by ADV at the thalweg and lower part of outer bank positions, suggesting that erosion did not occur at these locations during the T4 tidal cycle.

Previous studies have shown that the fetch length, wind speed, and duration determine the size of wind-generated waves (Bouws et al., 1996). This effect is more pronounced on shallow tidal flats, where field observations and numerical simulations have revealed that under certain wind speeds, the bottom shear stress due to wind waves changes with water depth. The shear stress increases continuously from the water surface to a certain depth threshold, and then decreases beyond that threshold (Fagherazzi et al., 2006). Further subdivision indicates that during ebb tide when the water depth is between mean sea level and mean low tide level, the reduction in water depth relative to wind direction and fetch length determines the magnitude of shear stress. During flood tide when the water depth is between mean sea level and mean high tide level, the fetch length plays a more significant role in determining shear stress (Fagherazzi and Wiberg, 2009). The water depth threshold is positively correlated with wind speed, with higher wind speeds corresponding to higher thresholds (Mariotti and Fagherazzi, 2013). Some scholars have observed that in weak tidal flats, a wind speed of 5 m/s and a fetch length of 5 km can significantly influence the bottom shear stress (Hunt et al., 2015). Wang et al. (2012) suggested that strong winds and long fetch lengths may lead to erosion of the broad intertidal mudflats in Jiangsu during autumn.

During the T4 semi-diurnal tidal period, the maximum wind speed ranged from 6.27 to 7.33 m/s, consistently blowing towards the shore in the direction of 59°-74° throughout the flood and ebb tide cycles. The persistent onshore winds resulted in an extended duration of the ebb tide during the T4 tidal period (Fig. 4a). On the mudflat, the tidal currents exhibited more scattered direction, while within tidal channels, the influence of the wind caused the tidal current direction during the T4 tidal period to transition from a significant east-west movement aligned with the channel to a more random and disorderly flow (Fig. 6). The tidal flat in the study area, as shown in Fig. 12, had a shoreline orientation of 45°, extending approximately 2.5 km from land to reach the near end of a small Yangkou channel with a depth of 10 m, and about 5 km from land to reach the far end of the Yangkou channel at 70°. The maximum water depth during the T4 tidal period was 2.5 m, and during low tide, the sustained wind speeds of around 7 m/s and the wind fetch length of 5 km significantly increased the bed shear stress at the mudflat location. As the water depth decreased, the shear stress further intensified, surpassing the critical shear stress of the mudflat, leading to erosion. In the tidal

channels, the presence of a channel with a maximum depth of approximately 1.4 m increased the water depth, preventing the wind from generating sufficient bed shear stress at the channel bottom, limiting the potential impact to the upper part of the shore parallel to the mudflat.

It can be observed that under normal weather conditions, changes in erosion and accretion on tidal flats do not necessarily occur during the peak flow velocities of the spring tides. The influence of wind conditions can lead to the generation of significant bed shear stress during the neap low tides, and wind speeds at appropriate angles can affect the geomorphology of tidal flats. Given the long perpendicular width of tidal flats in Jiangsu, which can offset contributions along the coastal length in the wind fetch, the impact of wind direction-determined fetch length on bed shear stress in Jiangsu tidal flats has yet to be further explored. However, this shaping effect is particularly significant in the tidal flats of Rudong.

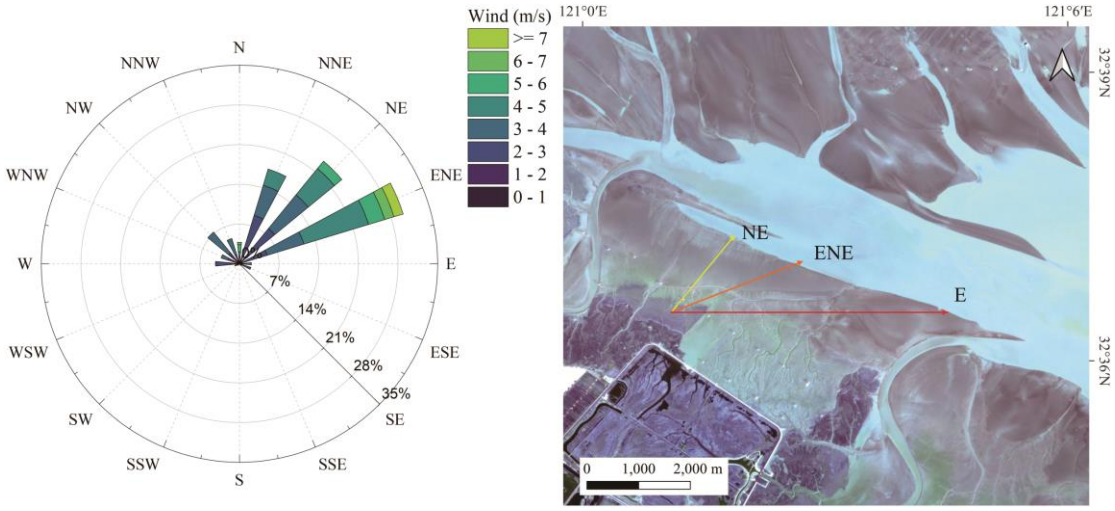

Fig. 12 Rudong wind rose diagrams and wind fetch lengths for the observation period.

Mechanisms of bank failure in a macro-tidal bare flat tidal channel

Gao et al. (2022) investigated the development process and mechanism of meandering channels in the intertidal flats of the region. The results indicate that the geomorphic evolution in this area may be more influenced by biogeomorphic factors related to other processes during the late stages of the tidal cycle rather than the lateral circulation induced by bend curvature during the flood tide. Building upon their work, the study further explores and elucidates the mechanism of bank slope

collapse in macro-tidal muddy intertidal flat channels.

During the observation period, at the same elevation within the channel, the suspended sediment concentration decreases successively along the outer bank-thalweg-inner bank, with the current velocity observed at the outer bank being greater than that at the thalweg. This is related to the location of the observation cross-section, which is situated at the bend crest of the meandering channel, as shown in Fig. 1. The flow field within the meander is constrained by the topography, generating lateral circulation driven by unbalanced vertical centrifugal forces and lateral pressure gradient forces (Ahnert, 1960; Solari, 2002; Fagherazzi et al., 2004). In the current velocity observations within the channel, peak tidal velocities are observed below the bank-full depth, without the asymmetric peak phenomenon seen in salt marsh channels (French and Stoddart, 1992; Pethick, 1980; Fagherazzi et al., 2008), which is related to the different bed friction coefficients (Gao et al., 2022).

Field observations reveal fan-shaped collapse areas on the shoals and slopes of the channel. Three different forms of topographic changes in the channel's bank slopes can be observed in the point cloud data from TLS (Fig. 11). In cross-section A of the channel, the most noticeable topographic change is the retreat of the upper outer bank due to collapse, while acceleration occurs in the middle portion of the bank. This phenomenon is visually confirmed in on-site photographs (Fig. 13). Elliptical areas show impending collapse blocks with dense crab burrows upon magnification, while the rectangular boxes indicate collapsed blocks loosely piled on the bank.

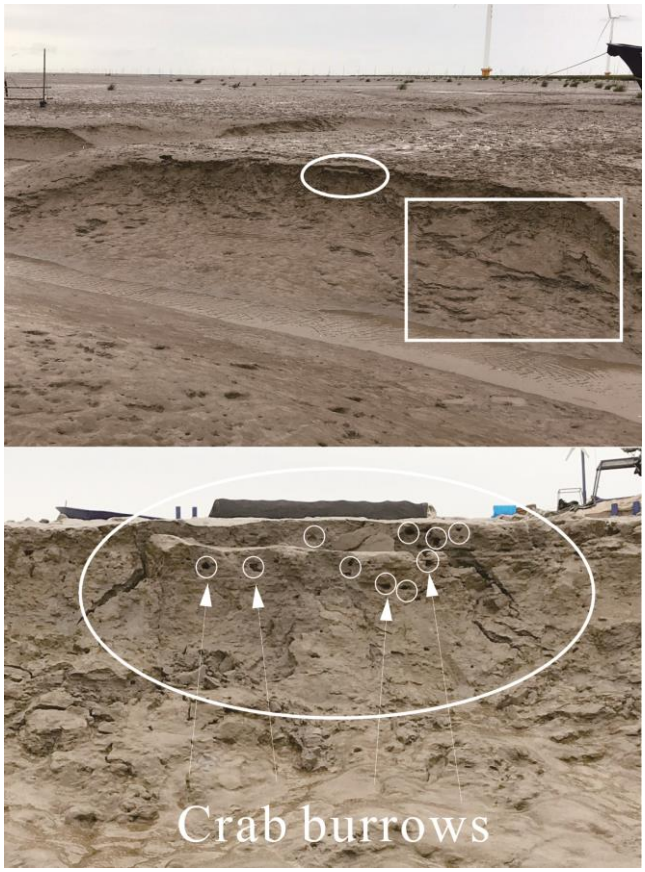

Fig. 13 Fan-shaped collapse area with crab burrows.

In cross-section B of the tidal channel, significant sediment acceleration has occurred on the outer bank, which is not located within the fan-shaped collapse zone, but consists of gentler slopes. No photographs were taken at cross-section C, but both the inner banks and outer banks of cross-section C contain fan-shaped collapse zones, and significant retrogressive collapse has also occurred.

The phenomenon of collapse in tidal channels has been observed in intertidal zones in other regions of the world (Barwis, 1978; Gabet, 1998; Whitehouse et al., 2000; Gong et al., 2018; Zhao et al., 2022). The bank collapse forms observed at Rudong mudflat are similar to wave-induced overturning collapses (Bendoni et al., 2014), but not entirely the same in terms of process and mechanism.

As shown in Fig. 14, field photos of tidal channel development at different stages in Rudong were selected. Figs. 14 (a, b, c, e) were taken in 2019, while Fig. 14d was taken in 2020 at the site of a fan-shaped collapse observed during the monitoring period. Figs. 14 (a, b, e) depict different locations of the same tidal creek, with Fig. 14a located at the far end of e, connecting to the main tidal channel, Fig. 14b being the source of the channel with a clear headcut, and Fig. 14b

representing a secondary channel developed in the middle of the tidal channel. Fig. 14c is situated in the main tidal channel connected to Fig. 14a, positioned more inland compared to the cross-section in 2020. Fig. 14d shows the seaward direction of the main tidal channel, the same channel as Fig. 14c, but wider and deeper.

By combining field photos at different stages, field observations, and previous research, a new mechanism for tidal channel bank slope erosion-protection can be proposed: (1) in the early stages of tidal channel development, the headcut of the gully will continuously erode upstream, with erosion locations related to micro-landforms on tidal flats, such as caves or small tidal marks (Perillo and Lribarne, 2003; Escapa et al., 2008; Le Minor et al., 2020). At this stage, the channel cuts below the main channel, creating deep V-shaped or U-shaped incisions at the eroded areas on the flat. The slopes on both sides of the channel are perpendicular to the tidal flat. (2) As the channel further develops, widening and deepening its profile, the steep slopes perpendicular to the tidal flat are not stable enough to support themselves during ebb tides, leading to sliding collapses in the channel. The sliding blocks will accumulate loosely at the lower part of the slope, causing the slope below the channel to become gentler (Gabet, 1998). (3) As the channel continues to develop, vertical banks in an unbalanced state will exhibit tension cracks. However, due to the increased scale of the channel, normal weather conditions do not provide enough hydrodynamic force to continuously erode the slopes of the tidal flat. Consequently, the loose accumulations at the lower part of the channel slope undergo diatom colonization, enhancing the erosion resistance of the loose accumulations in the middle and lower parts of the channel bank (Grabowski et al., 2011). Simultaneously, with the changing tides, the deepening and widening of the channel increase the difference in water content between the top and bottom of the tidal flat, altering the mechanical properties and shear forces of the bank. As the base of the tension cracks is covered by algae, the blocks cannot collapse through sliding, leading to toppling collapses. (4) As the toppling collapses continue to a certain extent, the accumulations in the middle and lower parts of the tidal flat bank cause the bank to decrease below the critical erosion threshold, reaching a new dynamic equilibrium.

In this proposed mechanism, the collapse of tidal channels is jointly controlled by multiple factors: developmental stage, physical properties, topographic changes, and biological factors. This can be summarized schematically in Fig. 15. For newly developing small tidal gullies, channel development mainly occurs through widening and deepening, with most slopes having vertical

banks. For medium-sized creeks (width 1-2 m, depth less than 1 m), channel collapse primarily occurs in the form of sliding. For large channels (width greater than 5 m, depth greater than 1 m), due to the influence of biological activity, channel collapse mainly occurs in the form of toppling. Crab activity can induce the appearance of tension cracks, while during peak tidal flow below the intertidal level, bank collapse may occur during strong wind and wave periods. Due to diatom growth and reduced slope gradient in the lower part of the bank, collapse occurs mainly in the form of toppling. Part of the eroded collapse block is loosely accumulated in the lower part of the channel, while the other part is either washed down to the channel bed for deposition or transported away. The new loose accumulation undergoes reshaping after several weak hydrodynamic tidal cycles, and new diatom may regrow.

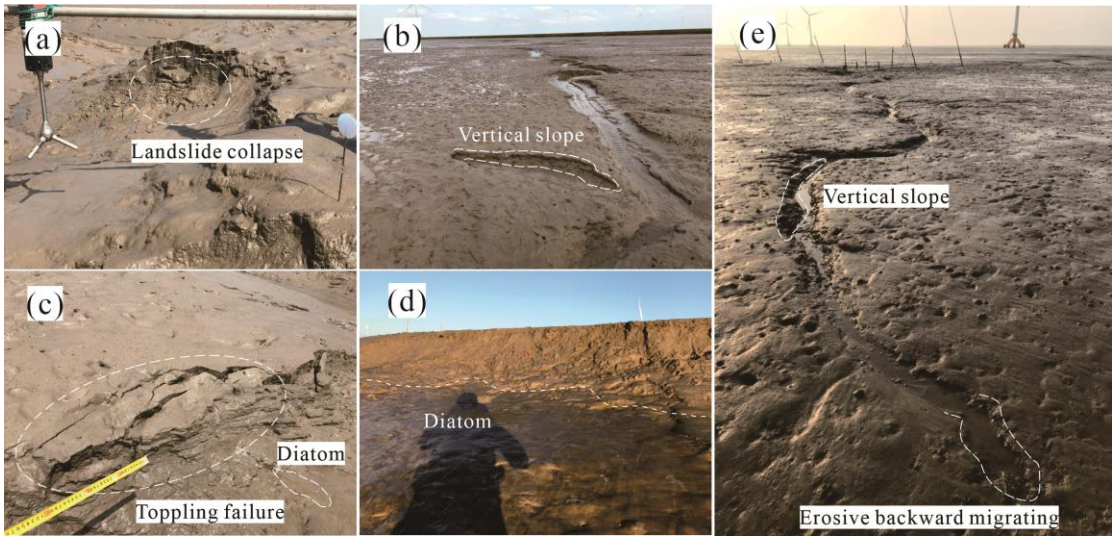

Fig. 14 Field photographs of tidal channels at different stages of development. (a) Sliding failure of medium-sized tidal creeks (8-June-2019); (b) Development of secondary tidal gullies in small tidal gullies, with the vertical slope to the tidal flat (4-June-2019); (c) Toppling failure of the bank of large tidal channels (8-June-2019); (d) The lower part of the bank of large tidal channels covered by diatom (13-October-2020); (e) Headcut erosion of small tidal gullies, with the vertical slope to the tidal flat (4-June-2019).

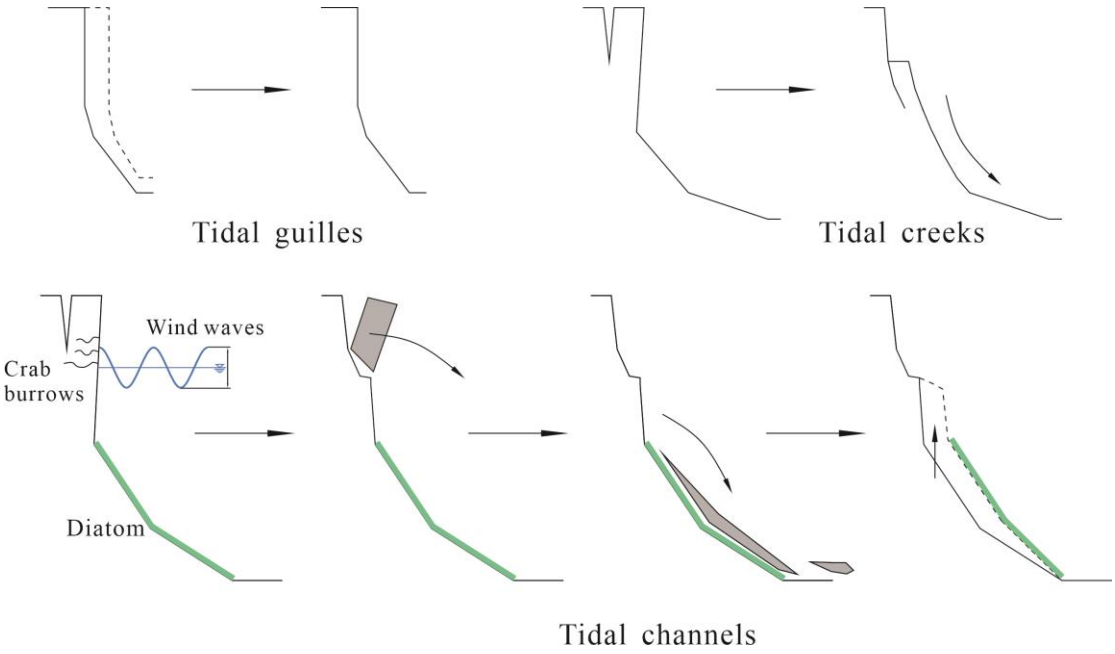

Fig. 15 Mechanisms of bank failure in different types of tidal channels

Conclusions

In this study, we utilized field observations to monitor the waves, tidal currents, suspended sediment concentrations, and geomorphological changes of intertidal zones under normal weather conditions. The main findings and insights are as follows:

(1) Wind conditions and fetch length are important factors influencing the erosion and accretion of intertidal zones under normal weather conditions, with stronger erosion resistance observed in the deep channels and lower part of the bank. Peak tidal currents within the channels occur during stages below the bankfull depth. The persistent wave oscillations below the bankfull depth at the observed cross-section of the channels may be the primary cause of erosion on the channel banks.

(2) Three different processes of channel slope erosion were identified in the field: ① Upstream erosion in small gullies with widening and deepening, leading to vertical slope to tidal flats. ② sliding collapse in medium-sized tidal creeks. ③ Due to biological disturbances, large channels experience cracking at the top of the bank under hydrodynamic forces, forming unstable blocks. These blocks are protected at their base by diatom cover, making them less prone to sliding collapse and more likely to experience toppling collapse. After toppling collapse, some loose deposits remain in the lower and middle parts of the bank for reshaping, while others are washed into the channel

by water flow.

Acknowledgements

We warmly acknowledge our colleagues Dr. Wei Feng, Yupeng Pan, Dongyun Wei, Hanzhen Shi, Yaping Mei, and Jianxiong Sun for their assistance in the field observations and laboratory works.

Funding

This study was funded by the National Natural Science Foundation of China (NSFC 41530962 and 41625021).

Conflict of interest

The authors declare that there is no conflict ofinterest with third parties.

Author contributions

Zhenqiao Liu：Conceptualization, research plan, data collection and analysis, writing—original draft preparation; Liming Xue: Conceptualization, data collection and analysis, writing—original draft preparation; Chao Gao: research plan, data collection and analysis, writing—original draft preparation; Benwei Shi: data collection and analysis, supervision; Ya Ping Wang: research plan, writing—reviewing and editing, supervision; Shu Gao: writing—reviewing and editing, supervision. All authors discussed the results and contributed to the final manuscript. All authors have read and agreed to the published version of the manuscript.

Reference

Ahnert F. Estuarine meanders in the Chesapeake Bay area[J]. Geographical review, 1960, 50(3):

390-401.

Allen J R L. Morphodynamics of Holocene salt marshes: a review sketch from the Atlantic and Southern North Sea coasts of Europe[J]. Quaternary Science Reviews, 2000, 19(12): 1155-1231.

Barwis J H. Sedimentology of some South Carolina tidal-creek point bars, and a comparison with their fluvial counterparts[J]. 1977.

Bendoni M, Francalanci S, Cappietti L, et al. On salt marshes retreat: Experiments and modeling toppling failures induced by wind waves[J]. Journal of Geophysical Research: Earth Surface, 2014, 119(3): 603-620.

Bouws E, Jannink D, Komen G J. The increasing wave height in the North Atlantic Ocean[J]. Bulletin of the American Meteorological Society, 1996, 77(10): 2275-2278.

Brivio L, Ghinassi M, D'Alpaos A, et al. Aggradation and lateral migration shaping geometry of a tidal point bar: An example from salt marshes of the Northern Venice Lagoon (Italy)[J]. Sedimentary Geology, 2016, 343: 141-155.

Cao Z D, Yang S S. Analysis of probability of channel rapid siltation of Yangkou Harbour[J]. Journal of Waterway and Harbor, 2006, (01): 9-13. (in chinese)

Chen Y, Dong J, Xiao X, et al. Land claim and loss of tidal flats in the Yangtze Estuary[J]. Scientific Reports, 2016, 6(1): 24018.

Christiansen C, Vølund G, Lund-Hansen L C, et al. Wind influence on tidal flat sediment dynamics: Field investigations in the Ho Bugt, Danish Wadden Sea[J]. Marine Geology, 2006, 235(1-4): 75-86.

Colosimo I, de Vet P L M, van Maren D S, et al. The impact of wind on flow and sediment transport over intertidal flats[J]. Journal of Marine Science and Engineering, 2020, 8(11): 910.

Day J W, Britsch L D, Hawes S R, et al. Pattern and process of land loss in the Mississippi Delta: a spatial and temporal analysis of wetland habitat change[J]. Estuaries, 2000, 23: 425-438.

De Swart H E, Zimmerman J T F. Morphodynamics of tidal inlet systems[J]. Annual review of fluid mechanics, 2009, 41: 203-229.

Dean R G, Dalrymple R A. Water wave mechanics for engineers and scientists[M]. world scientific publishing company, 1991.

Dyer K R, Christie M C, Manning A J. The effects of suspended sediment on turbulence within an estuarine turbidity maximum[J]. Estuarine, Coastal and Shelf Science, 2004, 59(2): 237-248.

Escapa M, Perillo G M E, Iribarne O. Sediment dynamics modulated by burrowing crab activities in contrasting SW Atlantic intertidal habitats[J]. Estuarine, Coastal and Shelf Science, 2008, 80(3): 365-373.

Fagherazzi S, Carniello L, D'Alpaos L, et al. Critical bifurcation of shallow microtidal landforms in tidal flats and salt marshes[J]. Proceedings of the National Academy of Sciences, 2006, 103(22): 8337-8341.

Fagherazzi S, Gabet E J, Furbish D J. The effect of bidirectional flow on tidal channel planforms[J]. Earth Surface Processes and Landforms: The Journal of the British Geomorphological Research Group, 2004, 29(3): 295-309.

Fagherazzi S, Hannion M, D'Odorico P. Geomorphic structure of tidal hydrodynamics in salt marsh creeks[J]. Water resources research, 2008, 44(2).

Fagherazzi S, Wiberg P L, Temmerman S, et al. Fluxes of water, sediments, and biogeochemical compounds in salt marshes[J]. Ecological Processes, 2013, 2: 1-16.

Fagherazzi S, Wiberg P L. Importance of wind conditions, fetch, and water levels on wave‐generated shear stresses in shallow intertidal basins[J]. Journal of Geophysical Research: Earth Surface, 2009, 114(F3).

Fan D, Li C, Archer A W, et al. Temporal distribution of diastems in deposits of an open-coast tidal flat with high suspended sediment concentrations[J]. Sedimentary Geology, 2002, 152(3-4): 173-181.

Finotello A, Lanzoni S, Ghinassi M, et al. Field migration rates of tidal meanders recapitulate fluvial morphodynamics[J]. Proceedings of the National Academy of Sciences, 2018, 115(7): 1463-1468.

French J R, Stoddart D R. Hydrodynamics of salt marsh creek systems: Implications for marsh morphological development and material exchange[J]. Earth surface processes and landforms, 1992, 17(3): 235-252.

Friedrichs C T, Perry J E. Tidal salt marsh morphodynamics: a synthesis[J]. Journal of Coastal Research, 2001: 7-37.

Gabet E J. Lateral migration and bank erosion in a saltmarsh tidal channel in San Francisco Bay, California[J]. Estuaries, 1998, 21(4): 745-753.

Gabet E J. Lateral migration and bank erosion in a saltmarsh tidal channel in San Francisco

Bay, California[J]. Estuaries, 1998, 21(4): 745-753.

Gao C, Finotello A, D'Alpaos A, et al. Hydrodynamics of Meander Bends in Intertidal Mudflats: a Field Study From the Macrotidal Yangkou Coast, China[J]. Water Resources Research, 2022, 58(12): e2022WR033234.

Gao S, Zhu D K. The profile of Jiangsu's mud coast[J]. Journal of Nanjing University (Natural Sciences Edition), 1988, 24(1): 75-84. (in chinese)

Gao S. Geomorphology and sedimentology of tidal flats[M]//Coastal wetlands. Elsevier, 2018: 359-381.

Ghinassi M, D'alpaos A, Gasparotto A, et al. Morphodynamic evolution and stratal architecture of translating tidal point bars: Inferences from the northern Venice Lagoon (Italy)[J]. Sedimentology, 2018, 65(4): 1354-1377.

Gong Z, Zhao K, Zhang C, et al. The role of bank collapse on tidal creek ontogeny: A novel process-based model for bank retreat[J]. Geomorphology, 2018, 311: 13-26.

Gong Z, Zhao K, Zhang C, et al. The role of bank collapse on tidal creek ontogeny: A novel process-based model for bank retreat[J]. Geomorphology, 2018, 311: 13-26.

Grabowski R C, Droppo I G, Wharton G. Erodibility of cohesive sediment: The importance of sediment properties[J]. Earth-Science Reviews, 2011, 105(3-4): 101-120.

Grandjean T J, Weenink R, van der Wal D, et al. Critical turbidity thresholds for maintenance of estuarine tidal flats worldwide[J]. Nature Geoscience, 2024: 1-6.

Green M O. Very small waves and associated sediment resuspension on an estuarine intertidal flat[J]. Estuarine, coastal and shelf science, 2011, 93(4): 449-459.

Hunt S, Bryan K R, Mullarney J C. The influence of wind and waves on the existence of stable intertidal morphology in meso-tidal estuaries[J]. Geomorphology, 2015, 228: 158-174.

Kelleway J J, Saintilan N, Macreadie P I, et al. Sedimentary factors are key predictors of carbon storage in SE Australian saltmarshes[J]. Ecosystems, 2016, 19: 865-880.

Kim S C, Friedrichs C T, Maa J P Y, et al. Estimating bottom stress in tidal boundary layer from acoustic Doppler velocimeter data[J]. Journal of Hydraulic Engineering, 2000, 126(6): 399-406.

Kularatne S, Pattiaratchi C. Turbulent kinetic energy and sediment resuspension due to wave groups[J]. Continental Shelf Research, 2008, 28(6): 726-736.

Le Minor M, Mullarney J C, Pilditch C A, et al. Crab burrow aspect ratio influences particle capture rates on intertidal sandflats[J]. Geo-Marine Letters, 2020, 40(2): 197-216.

Mann K H. Ecology of coastal waters: with implications for management[M]. John Wiley & Sons, 2009.

Marani M, Lanzoni S, Zandolin D, et al. Tidal meanders[J]. Water Resources Research, 2002, 38(11): 7-1-7-14.

Mariotti G, Fagherazzi S. Wind waves on a mudflat: The influence of fetch and depth on bed shear stresses[J]. Continental Shelf Research, 2013, 60: S99-S110.

Mudd S M, D'Alpaos A, Morris J T. How does vegetation affect sedimentation on tidal marshes? Investigating particle capture and hydrodynamic controls on biologically mediated sedimentation[J]. Journal of Geophysical Research: Earth Surface, 2010, 115(F3).

Murray N J, Phinn S R, DeWitt M, et al. The global distribution and trajectory of tidal flats[J]. Nature, 2019, 565(7738): 222-225.

Perillo G M E, Gao S, Cuadrado D G, 2024. Tidal flats: geomorphology and dynamics. In: Uncles R J, Mitchell S, French J (editors), Treatise on estuarine and coastal science (2nd edition), Amsteram: Elsevier, v.2, 809-842.

Perillo G M E, Iribarne O O. New mechanisms studied for creek formation in tidal flats: from crabs to tidal channels[J]. Eos, Transactions American Geophysical Union, 2003, 84(1): 1-5.

Pethick J S. Velocity surges and asymmetry in tidal channels[J]. Estuarine and Coastal Marine Science, 1980, 11(3): 331-345.

Renshun Z. Suspended sediment transport processes on tidal mud flat in Jiangsu Province, China[J]. Estuarine, Coastal and Shelf Science, 1992, 35(3): 225-233.

Riegl, 2020. Riegl VZ-4000 Specificaitons. http://www.riegl.com/uploads/tx_pxpriegldownloads/RIEGL_VZ-4000_Datasheet_2020-09-14.pdf. Accessed 10 May 2024.

Salehi M, Strom K. Measurement of critical shear stress for mud mixtures in the San Jacinto estuary under different wave and current combinations[J]. Continental Shelf Research, 2012, 47: 78-92.

Shen Q, Zhu Q, Liu S, et al. Sedimentation of cohesive sediments at the subtidal flat affected by wind wave in high turbidity estuary[J]. Frontiers in Marine Science, 2023, 9: 1045335.

Shi B W, Yang S L, Wang Y P, et al. Role of wind in erosion‐accretion cycles on an estuarine mudflat[J]. Journal of Geophysical Research: Oceans, 2017, 122(1): 193-206.

Shi B, Wang Y P, Yang Y, et al. Determination of critical shear stresses for erosion and deposition based on in situ measurements of currents and waves over an intertidal mudflat[J]. Journal of Coastal Research, 2015, 31(6): 1344-1356.

Solari L, Seminara G, Lanzoni S, et al. Sand bars in tidal channels Part 2. Tidal meanders[J]. Journal of Fluid Mechanics, 2002, 451: 203-238.

Soulsby R L, Clarke S. Bed shear-stress under combined waves and currents on smooth and rough beds (TR 137)[J]. 2005.

Soulsby R L, Humphery J D. Field observations of wave-current interaction at the sea bed[M]//Water wave kinematics. Dordrecht: Springer Netherlands, 1990: 413-428.

Soulsby R L. Bed shear-stresses due to combined waves and currents[J]. Advances in coastal morphodynamics, 1995.

Spencer K L, Harvey G L. Understanding system disturbance and ecosystem services in restored saltmarshes: Integrating physical and biogeochemical processes[J]. Estuarine, Coastal and Shelf Science, 2012, 106: 23-32.

Stefanon L, Carniello L, D'Alpaos A, et al. Signatures of sea level changes on tidal geomorphology: Experiments on network incision and retreat[J]. Geophysical Research Letters, 2012, 39(12).

Talke S A, Stacey M T. Suspended sediment fluxes at an intertidal flat: The shifting influence of wave, wind, tidal, and freshwater forcing[J]. Continental Shelf Research, 2008, 28(6): 710-725.

Temmerman S, Govers G, Wartel S, et al. Modelling estuarine variations in tidal marsh sedimentation: response to changing sea level and suspended sediment concentrations[J]. Marine Geology, 2004, 212(1-4): 1-19.

Temmerman S, Horstman E M, Krauss K W, et al. Marshes and mangroves as nature-based coastal storm buffers[J]. Annual Review of Marine Science, 2023, 15: 95-118.

Temmerman S, Kirwan M L. Building land with a rising sea[J]. Science, 2015, 349(6248): 588-589.

Wang P. Principles of sediment transport applicable in tidal environments[M]//Principles of tidal sedimentology. Dordrecht: Springer Netherlands, 2011: 19-34.

Wang Y P, Gao S, Jia J, et al. Sediment transport over an accretional intertidal flat with influences of reclamation, Jiangsu coast, China[J]. Marine Geology, 2012, 291: 147-161.

Wang Y. Radiative sandy ridge field on continental shelf of the Yellow Sea[J]. China Environmental Science Press, 2002.

Wang Y. The mudflat system of China[J]. Canadian Journal of Fisheries and Aquatic Sciences, 1983, 40(S1): s160-s171.

Whitehouse R J S, Bassoullet P, Dyer K R, et al. The influence of bedforms on flow and sediment transport over intertidal mudflats[J]. Continental Shelf Research, 2000, 20(10-11): 1099-1124.

Whitfield A K. The role of seagrass meadows, mangrove forests, salt marshes and reed beds as nursery areas and food sources for fishes in estuaries[J]. Reviews in Fish Biology and Fisheries, 2017, 27(1): 75-110.

Xie W, He Q, Zhang K, et al. Application of terrestrial laser scanner on tidal flat morphology at a typhoon event timescale[J]. Geomorphology, 2017, 292: 47-58.

Xin P, Wilson A, Shen C, et al. Surface water and groundwater interactions in salt marshes and their impact on plant ecology and coastal biogeochemistry[J]. Reviews of Geophysics, 2022, 60(1): e2021RG000740.

Yang S L, Friedrichs C T, Shi Z, et al. Morphological response of tidal marshes, flats and channels of the outer Yangtze River mouth to a major storm[J]. Estuaries, 2003, 26: 1416-1425.

Zhang H, Zhao L, Du W, et al. Research on the Limit Values of Reclamation Based on Ecological Security: A Case Study of Tongzhou Bay in Rudong, Jiangsu Province[J]. International Journal of Environmental Research and Public Health, 2022, 19(14): 8301.

Zhao B, Liu Y, Wang L, et al. Stability evaluation of tidal flats based on time-series satellite images: A case study of the Jiangsu central coast, China[J]. Estuarine, Coastal and Shelf Science, 2022, 264: 107697.

Zhao K, Coco G, Gong Z, et al. A review on bank retreat: Mechanisms, observations, and modeling[J]. Reviews of Geophysics, 2022, 60(2): e2021RG000761.

Zhao Y Y, Gao S. Simulation of Tidal Flat Sedimentation in Response to Typhoon-induced Storm Surges: A case study from Rudong Coast, Jiangsu, China[J]. Acta Sedimentologica Sinica, 2015, 33(01): 79-90. (in chinese)

Zheng J, Wang J, Zhou C, et al. Numerical simulation of typhoon-induced storm surge along Jiangsu coast, Part II: Calculation of storm surge[J]. Water Science and Engineering, 2017, 10(1): 8-16.

Zhu D K, Xu T G. The cast development and exploit of middle Jiangsu[J]. Journal of Nanjing University (Natural Sciences Edition), 1982, 03: 799-818. (in chinese)

Zhu Q, Van Prooijen B C, Wang Z B, et al. Bed shear stress estimation on an open intertidal flat using in situ measurements[J]. Estuarine, Coastal and Shelf Science, 2016, 182: 190-201.

Zhu Q, Xing F, Wang Y P, et al. Hidden delta degradation due to fluvial sediment decline and intensified marine storms[J]. Science Advances, 2024, 10(18): eadk1698.